In situ growth of Nanoparticles through Control of Nonstoichiometry

Authors: Dragos Neagu[1]*, George Tsekouras[1,2], David N. Miller[1], Hervé Ménard[3] and John T.S. Irvine[1]*

Affiliations:

[1]University of St Andrews, St. Andrews, KY16 9ST, Scotland, United Kingdom.

G.T. formerly at address [1], currently at:

[2]Laboratory for High Performance Ceramics, Swiss Federal Laboratories for Materials Science and Technology, Überlandstrasse 129, 8600 Dübendorf, Switzerland

[3]Sasol Technology (UK) Ltd. St. Andrews, KY16 9ST, Scotland, United Kingdom.

*Correspondence to: dn67@st-andrews.ac.uk, jtsi@st-andrews.ac.uk

Abstract

Surfaces decorated with uniformly dispersed catalytically active nanoparticles play a key role in many fields including renewable energy and catalysis. These structures are typically prepared by deposition techniques, but alternatively they could be made by growing the nanoparticles in situ directly from the (porous) backbone support. Here we demonstrate that growing nano-size phases from perovskites can be controlled through judicious choice of composition, particularly by tuning deviations from the ideal ABO_3 stoichiometry. This non-stoichiometry facilitates a change in equilibrium position to make particle exsolution much more dynamic, enabling the preparation of compositionally diverse nanoparticles (i.e. metallic, oxides, or mixtures) and seems to afford unprecedented control over particle size, distribution and surface anchorage. The phenomenon is also shown to be strongly influenced

by surface reorganisation characteristics. The concept exemplified here may serve in the design and development of more sophisticated oxide materials with advanced functionality across a range of possible domains of application.

Introduction

The development of tailored functional materials consisting of catalytic nanoparticles dispersed on external surfaces or on the inner surface of porous crystals is of key importance in many fields including catalysis, photocatalysis and energy conversion and storage (e.g. fuel cells, electrolysis cells, batteries). Generally, both types of microstructure are produced through deposition techniques (e.g. physical vapor deposition[1,2] or chemical impregnation[3,4], respectively), in which the catalysts or the catalyst precursors are attached onto the surface during a thermal treatment. While these approaches are widely applied, they offer limited control over the size, distribution and anchorage of the deposited species, not only during preparation, but also during ageing, and may be time consuming and costly.

When perovskite oxides (ABO_3) are employed as supporting frameworks it has been shown that certain catalysts can be incorporated as cations on the B-site of the perovskite lattice under oxidizing conditions and partly exsolved as nanoparticles upon subsequent reduction, thus opening the possibility of in situ growth of catalysts[5] (Figure 1a). As compared to traditional deposition techniques, this process has been shown to produce finer and better distributed catalyst nanoparticles, is more time- and cost-effective (that is, it does not require multiple "deposition" steps or expensive precursors), its reversibility means that catalyst agglomeration may be avoided through re-oxidation, thus greatly enhancing the lifetime of the catalyst[5,6].

So far, this concept has only been demonstrated for A to B stoichiometric perovskites (A/B = 1) and only for a limited number of easily reducible, catalytically active cations (Ni^{2+}, Ru^{2+},

Rh^{4+}, Pd^{4+} and Pt^{4+} – see Supplementary Figure S1), because the exsolution phenomenon is believed to be exclusively driven by the ease with which these cations reduce to metals[6–10]. Moreover, in the majority of these systems, exsolutions occur preferentially within the bulk rather than on the surface, rendering most of the nano-particles inaccessible for catalysis and thus decreasing the overall effectiveness of the approach[11]. Recently we found that harder-to-reduce cations can also be exsolved and, additionally, exsolutions emerge preferentially on the surface when highly A-site deficient perovskites (A/B < 1) are employed (e.g. $TiO_{2-\delta}$ exsolutions from $La_{0.4}Sr_{0.4}TiO_3$)[12]. Thus, A-site deficiency could serve as a general driving force for triggering B-site exsolution to produce a wider range of nanoparticle compositions with superior surface distribution and coverage. Moreover, A-site deficiency (henceforth denoted α, in e.g. $A_{1-\alpha}BO_3$) is the natural choice for designing systems that exsolve the B-site since in these systems exsolution acts to locally revert the perovskite towards a stable, "defect-free", ABO_3 stoichiometry. In initially stoichiometric compositions exsolution is typically accompanied by undesirable A-site cation containing phases (Figure 1b)[5]

Here we investigate the contribution of various factors for the in situ growth of nanoparticles from perovskites, and find that perovskite nonstoichiometry emerges as instrumental in this phenomenon. We also illustrate the thought process which enables one to tune nonstoichiometry and thus tailor particle growth for a palette of relevant applications.

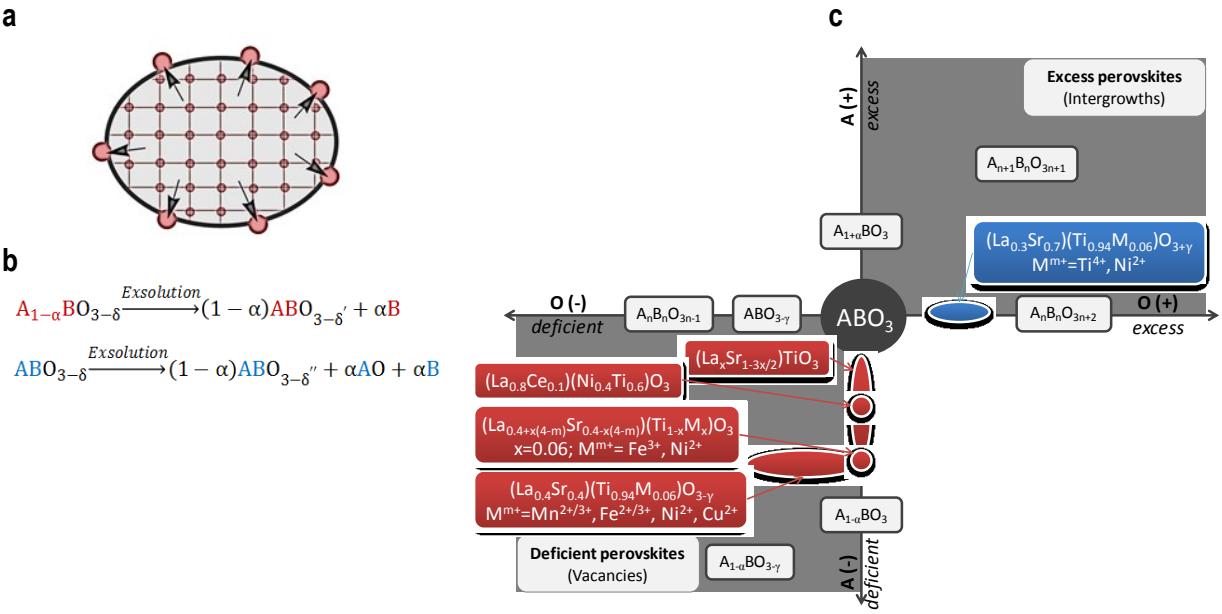

Figure 1 | Diagrams anticipating the key role of perovskite nonstoichiometry for in situ growth of nanoparticles. (a) Schematic representation of in situ exsolution of catalysts from a particle. In oxidizing conditions catalytically active species typically reside on the B-site perovskite sublattice as cations (small red dots inside the particle). Upon reduction, B-site species closer to the surface exsolve as nanoparticles (larger red circles), effectively decorating the outer surface of the parent perovskite particle. (b) Perovskites with A-site deficiency are anticipated to be more suitable for promoting the exsolution of B-site species as compared to cation stoichiometric perovskites (c) When the perovskite nonstoichiometry landscape is represented in a Cartesian plot (x and y axes corresponding to oxygen and A-site nonstoichiometry, respectively), deficient and excess perovskites appear to be diametrically opposed with respect to the defect-free ABO_3, thus outlining their observed antagonistic characteristics. In this plot, representative perovskites and perovskite-like series are outlined in grey (e.g. the Ruddlesden-Popper series $A_{n+1}B_nO_{3n+1}$, the oxygen deficient $A_nB_nO_{3n-1}$ brownmillerite type series, or the oxygen excess $A_nB_nO_{3n+2}$ homologous series), while the specific compositions prepared for this study are outlined in colored boxes (red: deficient perovskites and blue: excess perovskites).

Results and discussion

Studied systems in the context of perovskite nonstoichiometry

To provide a clear, visual distinction between the different nonstoichiometry classes, we associate them to the quadrants of a Cartesian plot having the O-site and A-site nonstoichiometry as x and y axis, respectively, and the defect-free ABO_3 as origin (Figure 1c). Through this representation we emphasize the diametrically opposed position of the *deficient* (A/B < 1 and/or O/B < 3) and *excess* perovskites (A/B > 1 and/or O/B > 3) with respect to the stoichiometric ABO_3, which anticipates their distinct structure and thus contrasting defect chemistries. The ideal perovskite structure (e.g. $SrTiO_3$) may be visualised as a continous 3D network of corner-sharing BO_6 octahedra, in which A-site cations occupy

the resulting cubo-octahedral cavities. Deficiency is achieved by creation of A, O-site *vacancies* while preserving overall octahedra connectivity [13–16].Excess, however, is accommodated, by alternating perovksite slabs with *intergrowth* regions (where the excess species reside), thus locally disrupting the continuity of the octahedra network (Supplementary Figure S2)[17–19].

We exemplify the exsolution phenomenon on compositions derived from the archetype perovskite, $SrTiO_3$, and make use of the exceptional ability of the perovskite lattice to accommodate dopants of different *size* (through tilting and/or deformation of the octahedra) and *charge* (by adopting deficient or excess stoichiometry), in order to tailor the cation constitution and nonstoichiometry. Thus, La^{3+} was substituted for Sr^{2+} in $SrTiO_3$, its higher charge compensated by extra oxygen to produce the A-site stoichiometric, oxygen excess series $La_ySr_{1-y}TiO_{3+y/2}$ or by A-site vacancies leading to the A-site deficient series $La_xSr_{1-3x/2}TiO_3$. We selected the member $y = 0.30$ for the oxygen excess series and members with $x \leq 0.4$ for the A-site deficient series to avoid the compositional domains where oxygen defects or A-site vacancies, respectively, start ordering[14,18,20]. We then attempted to replace 6% of the Ti^{4+} ions in some of these compositions with cations of interest to be exsolved, such as $Mn^{2+/3+}$, $Fe^{2+/3+}$, Ni^{2+}, Cu^{2+} and $Ce^{3+/4+}$. The full list is included in Figure 1c, outlining the position of the studied composition in the perovskite nonstoichiometry space and structural motif class.

Accommodation of cation substitution into the pervoskite structure

Where the size of the dopant and the host were similar (Supplementary Figure S3) we observed the formation of the perovskite phase (Figure 2a) and the size of the perovskite (pseudocubic) unit cell shifted in proportion to the size of the dopant (Figure 2b), thus confirming substitution for the systems $La_{0.4}Sr_{0.4}(Mn/Ni/Fe/Cu)_xTi_{1-x}O_{3-\gamma}$ ($\gamma = (4\text{-}m)\cdot x/2$, where m and x are the charge and stoichiometry of the dopant, respectively). Ce^{4+} proved to

be too large to allow substitution on the B-site (see Supplementary Figure S3), and thus we devised a new A-site deficient perovskite series in which Ce would occupy the A-site, $La_{1.6-2x}Ce_{2x-0.7}Ni_xTi_{1-x}O_3$, and successfully prepared the $x = 0.4$ member exhibiting perovskite structure (Supplementary Figure S5

All transition metal dopants employed in this study possess lower oxidation state compared to the host (Ti^{IV}), hence, upon substitution, the decrease in the average B-site charge is compensated by a decrease in oxygen stoichiometry. Consequently, oxygen excess decreases in A-site stoichiometric compounds, e.g. from $La_{0.3}Sr_{0.7}TiO_{3.15}$ to $La_{0.3}Sr_{0.7}Ni^{II}_{0.06}Ti_{0.94}O_{3.09}$, diminishing the frequency of intergrowths (Supplementary Figure S7), while the A-site deficient $La_{0.4}Sr_{0.4}TiO_3$ additionally becomes oxygen deficient after substitution, $La_{0.4}Sr_{0.4}M_{0.06}Ti_{0.94}O_{3-\gamma}$. The large concentration of built-in A-site vacancies coupled with the oxygen vacancies induced through doping may destabilize the perovskite lattice prohibiting the incorporation of all B-site cations provided through stoichiometry (e.g. traces of rutile were found in some samples, Figure 2a). In order to improve cation solubility in the presence of A-site vacancies, we sought to minimise the overall number of starting defects by compensating B-site doping by balancing the charge on the A-site rather than by oxide ion vacancies, but retaining $\alpha = 0.2$. As expected, the new formulations, $La_{0.4+2x}Sr_{0.4-2x}Ni_xTi_{1-x}O_3$ and $La_{0.4+x}Sr_{0.4+x}Fe_xTi_{1-x}O_3$, showed no rutile (Figure 2a and Supplementary Figure S6).

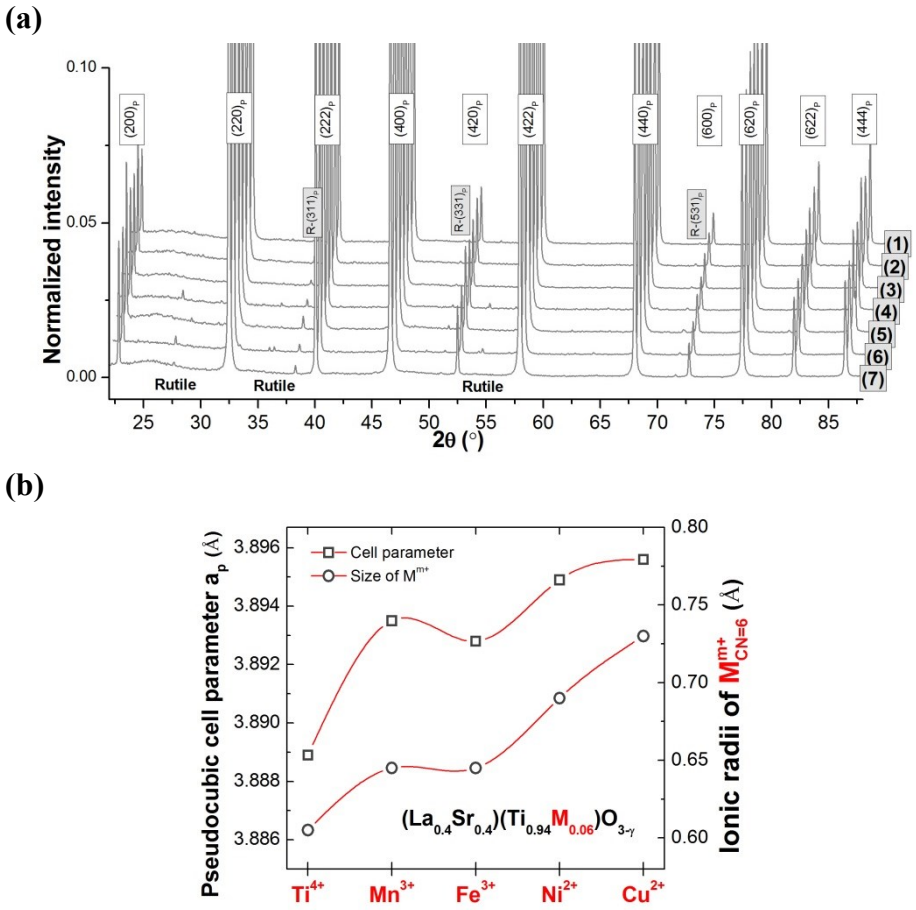

Figure 2 | Accommodation of B-site cation substitution into A-site deficient pervoskites. Substitution was confirmed by observation of characteristic perovskite reflections in XRD patterns and shifts in unit cell parameters proportional to dopant size. Dopant solubility is shown to be improved by tailoring perovskite stoichiometry towards minimizing initial defect types and/or concentration. (a) Room temperature XRD patterns of selected, as-prepared compositions with x = 0.06 B-site doping of M^{m+} cations, in the order of increasing cell size: (1) $La_{0.4}Sr_{0.4}TiO_3$ (2) $La_{0.4+x}Sr_{0.4-x}Fe_xTi_{1-x}O_3$, (3) $La_{0.4}Sr_{0.4}Mn_xTi_{1-x}O_{3-\gamma}$, (4) $La_{0.4}Sr_{0.4}Fe_xTi_{1-x}O_{3-\gamma}$, (5) $La_{0.4+2x}Sr_{0.4-2x}Ni_xTi_{1-x}O_3$, (6) $La_{0.4}Sr_{0.4}Ni_xTi_{1-x}O_{3-\gamma}$, (7) $La_{0.4}Sr_{0.4}Cu_xTi_{1-x}O_{3-\gamma}$. (b) Size of the unit cell compared to the size of the dopant M^{m+} for the as-prepared series $La_{0.4}Sr_{0.4}M_{0.06}Ti_{0.94}O_{3-\gamma}$, (ionic radii from Shannon[21]). The errors in unit cell parameters are smaller than the points used for plotting.

Nonstoichiometry-driven exsolutions

When reduced in the same conditions, the A-site deficient, oxygen stoichiometric composition $La_{0.52}Sr_{0.28}Ni_{0.06}Ti_{0.94}O_3$ develops numerous metallic Ni nanoparticles which uniformly cover the surface of the parent perovskite, whilst no particle growth was observed from the A-site stoichiometric, oxygen excess $La_{0.3}Sr_{0.7}Ni_{0.06}Ti_{0.94}O_{3.09}$ composition, even though both samples possess 6% Ni on the B-site (Figure 3). This experiment clearly indicates that A-site deficient perovskites are more prone to exolve B-site species than the oxygen excess ones and thus nonstoichiometry control can be employed to produce decorated perovskite surfaces with evenly distributed nanoparticles where traditional formulations

cannot. The complete absence of exsolutions from the above excess composition clearly shows that this is not a simple effect dependent only upon the presence of reducible ions in the lattice, but rather there is a strong influence coming from the equilibria between the lattice and surface.

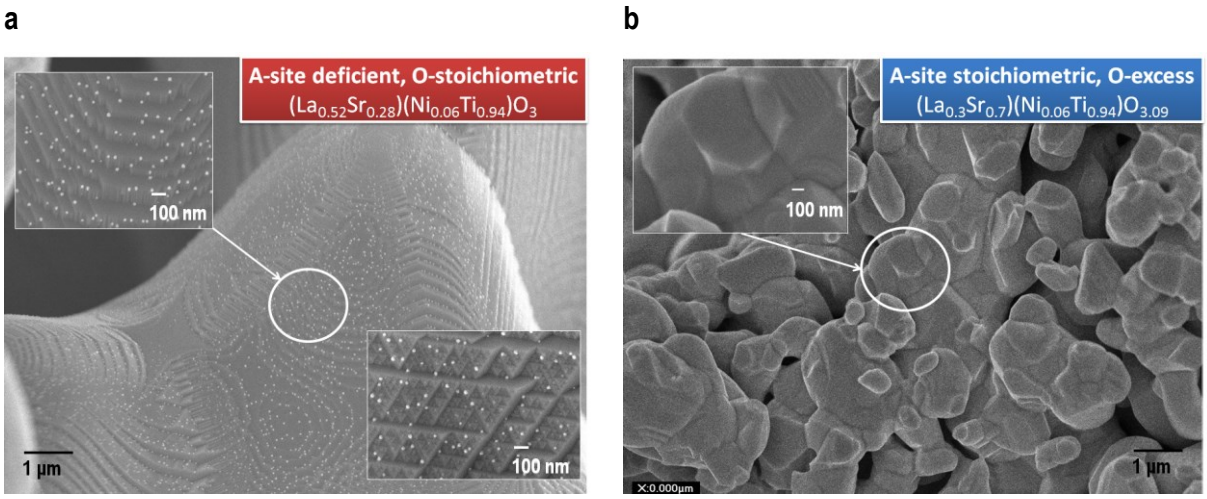

Figure 3 | The role of nonstoichiometry comparing the formation of exsolutions on stoichiometric and A-site deficient perovskites illustrated through SEM micrographs: (a) exsolutions from the initially A-site deficient, O-stoichiometric $La_{0.52}Sr_{0.28}Ni_{0.06}Ti_{0.94}O_3$ after reduction at 930 °C (20 h) in 5%H_2/Ar. (b) A-site stoichiometric, O-excess $La_{0.3}Sr_{0.7}Ni_{0.06}Ti_{0.94}O_{3.09}$ sample reduced at 930 °C (20 h) in 5%H_2/Ar indicating that no exsolution has occurred.

Thus, by reducing the A-site deficient compositions in which cation substitution was successful, we obtained exsolutes of diverse morphology and composition (Supplementary Figure S8). Based on the relative reducibility of the substituting cations (Supplementary Figure S1), the exsolutes are expected to consist of e.g.: $TiO_{2-\delta}$ from $La_{0.4}Sr_{0.4}TiO_3$; MnO_x from $La_{0.4}Sr_{0.4}Mn_{0.06}Ti_{0.94}O_{3-\gamma}$; Fe from $La_{0.4}Sr_{0.4}Fe_{0.06}Ti_{0.94}O_{3-\gamma}$; Ni from $La_{0.4}Sr_{0.4}Ni_{0.06}Ti_{0.94}O_{3-\gamma}$ and $La_{0.8}Ce_{0.1}Ni_{0.4}Ti_{0.6}O_3$. While Ni and Fe metallic exsolutions are easily detectable for example by XRD (Supplementary Figure S9), this is not as straightforward in the case of MnO_x or $TiO_{2-\delta}$ owing to the small dimensions of the nanoparticles and their lower number.

Influence of Stoichiometry upon Surface Morphology

Throughout this study it was found that generally the surface morphology of as-prepared, porous samples (i.e. equilibrated at ~1400 °C in air), henceforth referred to as the *native surface*, correlates with oxygen nonstoichiometry. O-deficient ($A_{1-\alpha}BO_{3-\gamma}$) compositions develop distinctive, terrace-like motifs (Figure 4a). The separation between adjacent terraces decreases significantly for O-stoichiometric ($A_{1-\alpha}BO_3$) compositions (Figure 3a) and eventually fades into a smooth surface for O-excess ($ABO_{3+\gamma}$) compositions (Figure 3b) Interestingly, the exsolution phenomenon occurs preferentially along the edge of these terraces, and typically never in the separation zone between them (as outlined in Figure 4a), implying that the native surface is structurally and/or compositionally inhomogeneous. .Consequently, samples which display smaller separation between terraces lead to more uniformly distributed exsolutions over the parent perovskite surface (Figure 3a vs. Figure 4a and Spplementary Figure-S8).

To understand the nature of the native surface and its role in the exsolution process a $La_{0.52}Sr_{0.28}Ni_{0.06}Ti_{0.94}O_3$ porous sample was studied in the presence and (partial) absence of surface structuring, by SEM and XPS (Figure 4b)-d). Instead of the expected $A_{0.8}BO_3$ stoichiometry, the native surface displayed considerable A, O-site excess, $A_{1.30}BO_{3.86}$ (Figure 4b). A-site surface enrichment in perovskites has been reported on numerous occasions for various systems[22–29], and also predicted by calculations[28]. Szot *et. al.* have shown that the A, O-site rich surface layer is usually, as the stoichiometry would imply, an A, O-site excess perovskite variant (i.e. Ruddlesden-Popper $A_{n+1}B_nO_{3n+1}$) and, at least in the case of $SrTiO_3$ single crystals, inherently forms during annealing in oxidizing conditions at high temperatures[26,30]. Thus, it is rather surprising that even A-site deficient perovskites develop surface A-site enrichment, but it is not surprising at all that this layer acts to locally suppress B-site exsolutions because it belongs to the excess perovskite nonstoichiometry class which we showed does not naturally promote B-site exsolutions. Alternatively,

compositions such as $A_{1.3}BO_{3.86}$ can be regarded as B-site deficient, i.e. $A_{1.01}B_{0.78}O_3$ which, again, would poor predisposition towards B-site exsolution at the surface.

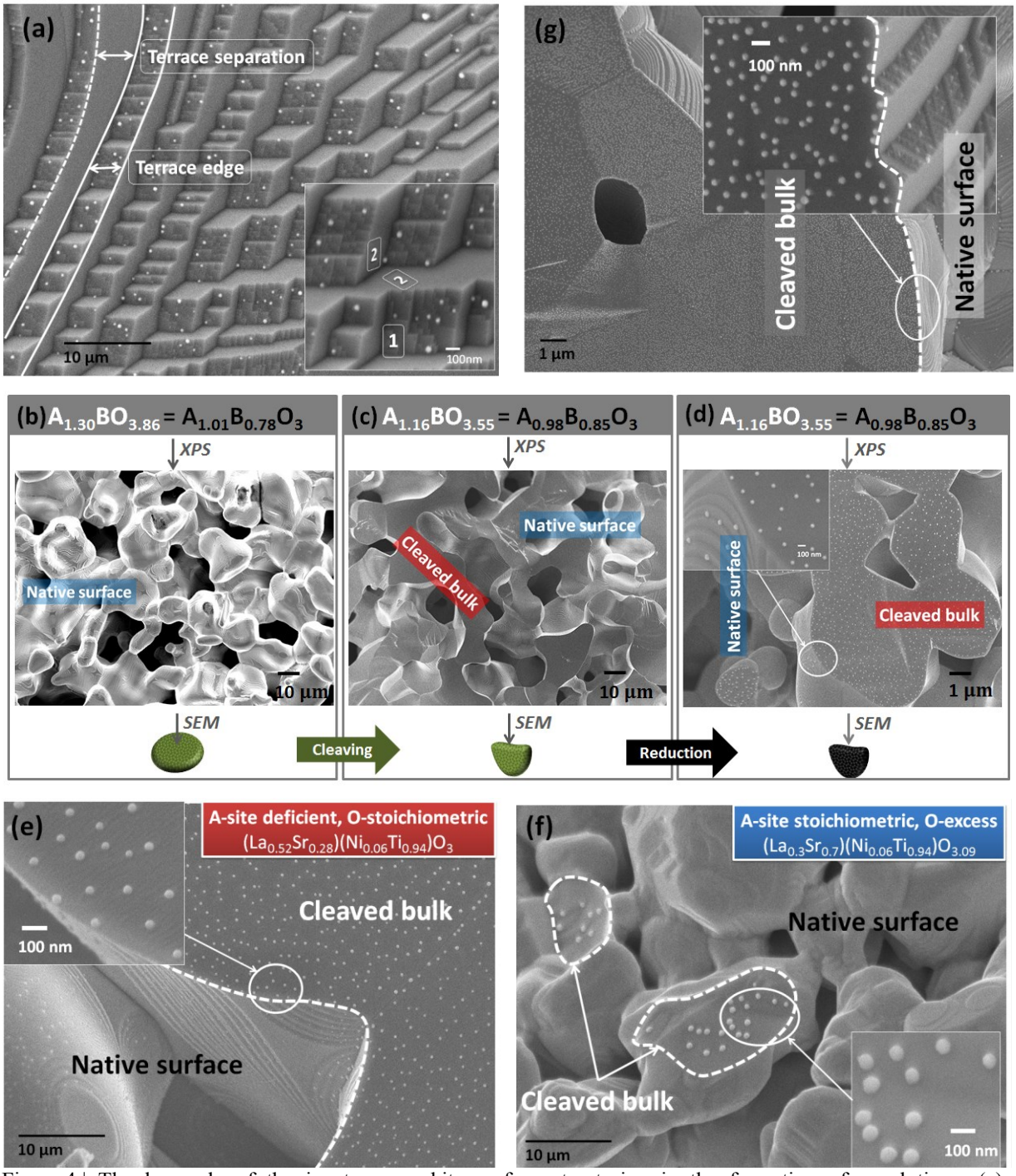

Figure 4 | The key role of the innate perovskite surface structuring in the formation of exsolutions. (a) Characteristic terracing of the native surface of an A-site deficient, O-deficient perovskite exemplified by $La_{0.4}Sr_{0.4}Ni_xTi_{1-x}O_{3-\gamma}$ (x = 0.03) reduced at 930 ˚C (20 h) in dry 5%H_2/Ar and then aged in 3%H_2O/5%H_2/Ar 900 ˚C (100 h). Nanoparticles preferentially grow on the terrace edge (marked with 1) rather than on the terrace separation region (marked with 2) Panels (b) to (d) present the microstructure (by SEM) and corresponding surface stoichiometry (by XPS) of a $La_{0.52}Sr_{0.28}Ni_{0.06}Ti_{0.94}O_3$ porous sample: (b) as-prepared (~1400 °C, air), i.e. native surface; (c) after cleaving, exposing the bulk-type surfaces with nominal stoichiometry; (d) after reducing the cleaved sample in the XPS in 5%H_2/Ar (30 minutes isothermal steps at 600, 700, 800 and 900 °C). (e) $La_{0.3}Sr_{0.7}Ni_{0.06}Ti_{0.94}O_{3.09}$, reduced at 900 °C (15 h) in 5%H_2/Ar; (f) $La_{0.52}Sr_{0.28}Ni_{0.06}Ti_{0.94}O_3$ reduced at 900 °C (15 h) in 5%H_2/Ar; (g) sample (f) aged in 3%H_2O/5%H_2/Ar at 900 °C for 60 h. Panels (e) and (g) illustrate that

the native surface terracing and associate local structure/composition severely hinders overall exsolution and may even fully suppress it as shown in panel (f).

The sample in Figure 4b was then cleaved, with most of the fracture occurring through the grains (Figure 4c), and thus revealing several 'bulk surfaces' of nominal $A_{0.8}BO_3$ stoichiometry. Correspondingly, the measured surface A-site excess decreases from $A_{1.3}BO_{3.86}$ to $A_{1.16}BO_{3.55}$. Upon reduction, the cleaved sample did not show any change in the overall stoichiometry (Figure 4d) and no metallic Ni could be detected by XPS, most likely due to the small relative sensitivity factor of Ni. However, SEM revealed that the exsolution process had occurred and most importantly that the nanoparticles were more abundant and much better distributed over the cleaved bulk surface compared to the native surface, implying that terrace structuring has a rather detrimental effect on the exsolution process by restricting particle nucleation to terrace edges (Figure 4d). Thus, a more representative perspective over the aptitude of different nonstoichiometry classes to produce exsolutions may be achieved by studying cleaved bulk surfaces (with nominal structure and stoichiometry) rather than the native surface.

When reduced under the same conditions, A-site deficient formulations are far superior in terms of producing small and uniformly distributed exsolutions over cleaved bulk surfaces compared to A-site stoichiometric analogues either when Ni is used as dopant (Figure 4e vs. Figure 4f) or when Ti solely occupies the B-site (Supplementary Figure S4). The fact that the A-site deficient systems display such a rich and evenly distributed growth of B-site exsolutions across the entire 'bulk terminated' surface suggests that the defect chemistry of this class innately favours nucleation of B-site containing phases virtually from everywhere on this surface.

Bulk surface studies also indicate that varying the concentration of A-site vacancies may be used to further tailor the exsolution phenomenon (Supplementary Figure S11). For the series $La_xSr_{1-3x/2}TiO_3$ ($\alpha = x/2$) an A-site deficiency of $\alpha = 0.2$ yields numerous and rather large

particles, which become finer and better distributed for $\alpha = 0.1$, and gradually disappear upon approaching stoichiometric ratios. This implies that at least in this system, a concentration of defects $\alpha = 0.1$ favours particle nucleation over growth which is desirable for producing fine and homogenously distributed nanoparticles.

Interestingly, by reducing some of the decorated surfaces (e.g. Figure 4d) for prolonged durations additional nanoparticles form, but no sign of nanoparticle clustering, or significant particle growth is observed, even though most particles are in nano-proximity with respect to each other, suggesting good anchoring of the nanoparticles onto the parent perovskite surface (Figure 4g).

An example of tailored nonstoichiometry

The stoichiometry of $La_{0.8}Ce_{0.1}Ni_{0.4}Ti_{0.6}O_3$ was designed to encompass a wide range of criteria which, throughout this study, were found to work synergistically towards producing superior exsolutions from perovskite native surfaces. An $\alpha = 0.1$ was chosen since this typically favours particle nucleation over particle growth, thus yielding fine, well distributed nanoparticles. Oxygen stoichiometry was fixed at 3 since this leads to smaller separation between terraces and hence better particle surface coverage. Sr^{2+} tends to promote the formation of Ruddlesden-Popper phases ($A_{n+1}B_nO_{3n+1}$) which are detrimental for particle nucleation and thus was replaced with $Ce^{4+/3+}$ which is additionally known for its interesting electro-catalytic properties. As shown in Figure 5a, upon reduction, this composition develops remarkably fine and well distributed exsolutions with outstanding surface coverage, providing proof of concept that nonstoichiometry and defect interactions can be tailored to enable advanced control over the exsolution phenomenon. Even when reduced at high temperatures (1000 °C) the Ni nanoparticles do not coalesce (Figure 5b, c). Moreover, it was found that Ni is not the only nano-size species present, but nanoparticles of fluorite-type structure, most likely reduced $CeO_{2-\delta}$ are also present (inset of Figure 5b). Notably, both Ni

and fluorite-type nano-phases appear to be coherent to some extent with the parent perovskite lattice (Supplemenary Figure S12). Interfaces such as these have been shown to exhibit remarkable properties[31].

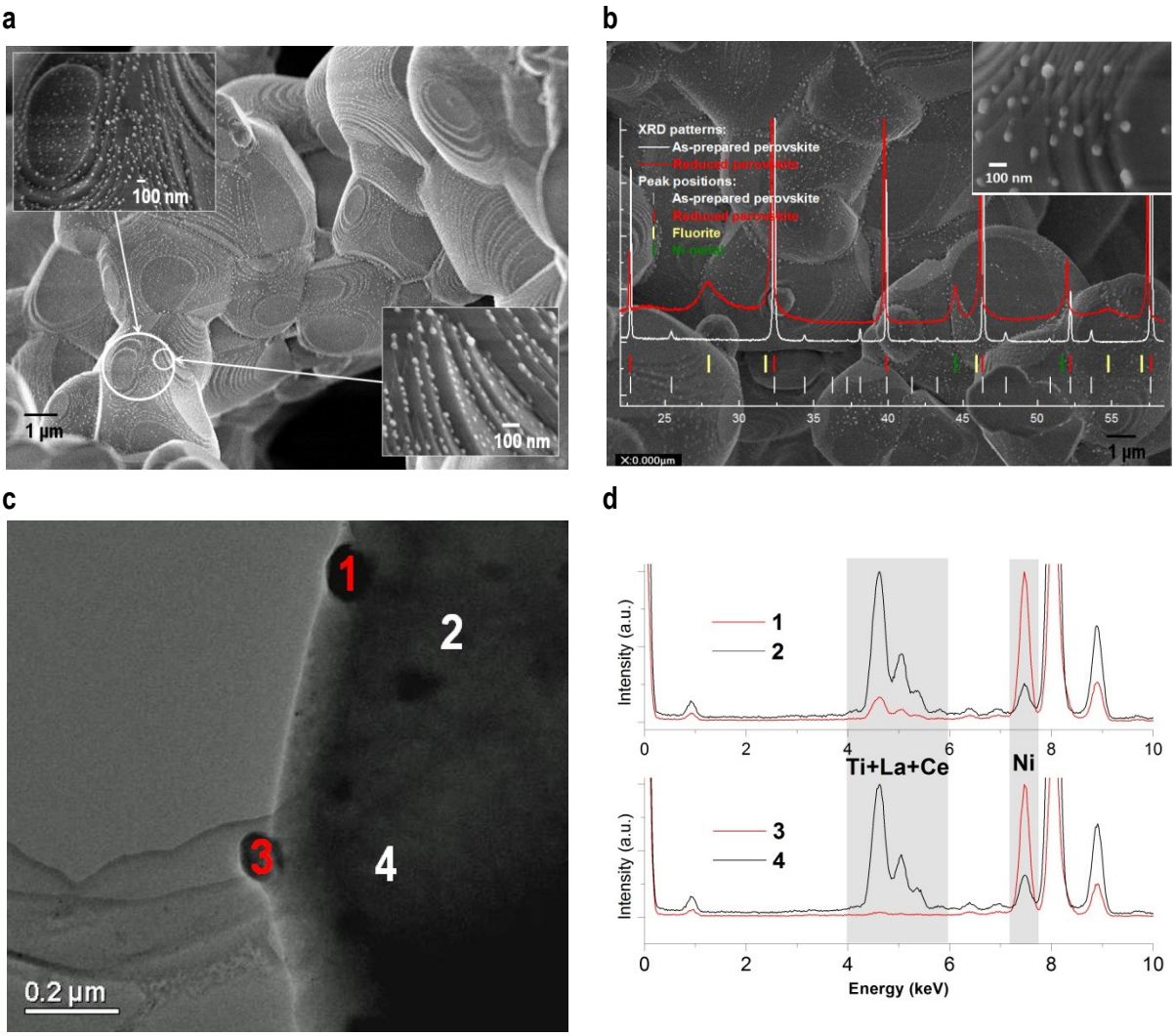

Figure 5 | Exsolutions of both Ni and CeO_2 in the nonstoichiometry-tailored system $La_{0.8}Ce_{0.1}Ni_{0.4}Ti_{0.6}O_3$. (a) after reduction in 5%H_2/Ar at 930 °C (20 h); (b) after reduction in 5%H_2/Ar at 1000 °C (20 h); the inset plot shows the corresponding XRD pattern; HRTEM (c) and EDS (d) analysis of surface nanoparticles of sample (b).

The role of A-site deficiency in driving B-site exolutions

By reducing an A-site deficient perovskite, e.g. $A_{1-\alpha}BO_3$, oxygen vacancies are introduced (δ = extent of the reduction, i.e. the number of oxygens removed per formula unit of perovskite, Figure 6a). The presence of vacancies on 2 of the 3 primitive sites destabilizes the perovskite lattice and may locally cause spontaneous exsolution of B-site species, in an attempt to re-establish stoichiometry across all the sites. This mechanism is translated into

point-defect reactions in Supplementary Figure S13, However, these should be interpreted with prudence since the defects discussed here diverge from the purest definition of point-defect given their high concentration and impact on the host lattice.

Alternatively, A, O-site deficient perovskite may be regarded as B-excess which would again explain the predisposition towards B-site exsolution. By contrast, in excess perovskites, the B-site will rarely be ‘under-coordinated’ or ‘exposed’, because of the intergrowths.

At an atomic scale, the removal of oxygen from a perovskite cell lacking the A-site cation may be visualized as locally secluding the B-site dopants from the main perovskite framework into an incipient exsolution (Figure 6a). Unit cells with occupied A-site are left unaltered, while the initial apparent “B-site excess” residing in the A-site deficient cells is expelled. This perspective illustrates how anchoring/coherence between the nucleating particles and parent perovskite may emerge based on reminiscent bonds between the two phases.

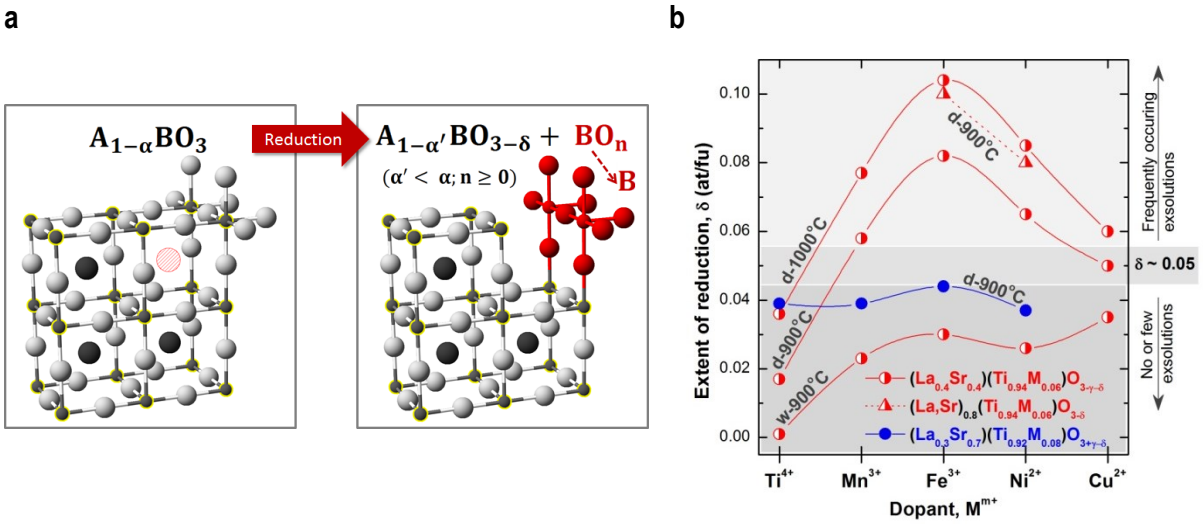

Figure 6 | Illustration of the role of A-site deficiency and extent of reduction in the exsolution of B-site species. (a) Schematic representation of the exsolution of B-site cations from A-site deficient perovskites. The O, B and A sites are depicted by silver, yellow contoured grey and dark grey spheres, respectively. An A-site vacancy is depicted by a red hashed circle. By removing oxygen from the A-site deficient unit cell through reduction, some B-sites are locally secluded from the parent perovskite into an incipient BO_n exsolution (depicted through the red group of atoms in the right panel). (b) The extent of reduction as a function of dopant for various systems and conditions, emphasizing the domains where the exsolution phenomenon was observed (from the native surface). Reduction was performed in dry ("d") or humidified ("w") reducing gas 3%H_2O/5%H_2/Ar at different temperatures; $(La,Sr)_{0.8}(Ti_{0.94}M_{0.06})O_{3-\delta}$ stands for $La_{0.46}Sr_{0.34}Fe_{0.06}Ti_{0.94}O_{3-\delta}$ and $La_{0.52}Sr_{0.28}Ni_{0.06}Ti_{0.94}O_{3-\delta}$. Data points for the series $La_{0.3}Sr_{0.7}M_{0.08}Ti_{0.92}O_{3+\gamma}$ from ref [32]. The errors are smaller than the points.

As suggested above, δ is expected play an important role in the occurrence of exsolutions, not only because it is a measure of the number of oxygen vacancies $V_O^{\cdot\cdot}$ created, but because it also correlates to the number of reduced B-site ions B_B' (not necessarily to the metallic state). This is expressed below by using the Kröger-Vink notation[33] for defects:

$$2B_B^x + O_O^x \rightleftharpoons 2B_B' + V_O^{\cdot\cdot} + \frac{1}{2}O_2$$

Indeed, we found that for systems with α = 0.2 exsolutions do not form at all or are sporadic when δ takes values below or around 0.05 (Figure 6b). This is the case for the samples which inherently do not reduce to high extents (e.g. $La_{0.4}Sr_{0.4}TiO_3$), or are exposed to insufficiently reducing conditions (e.g. $pO_2 > 10^{-16}$ atm, Supplementary Figure S8) or temperatures that are too low for sufficient reduction to occur. On the other hand, because δ depends on pO_2 and temperature, these parameters can be adjusted to cause exsolution in virtually any A-site deficient system.

Perspectives and implications of the phenomenon

We have been able to utilise control of composition and specifically degree of non-stoichiometry to tailor exsolution in a much more powerful manner that can be achieved by simple deposition techniques. The exsolution phenomenon is also critically controlled by the innate surface restructuring displayed by perovskites, which is however subject to manipulation through nonstoichiometry as well. The generality of the concept can be further refined by tuning the particle nucleation/growth balance through prudent adjustment of driving forces of 'intrinsic' nature (defect type and concentration, cation composition) or 'extrinsic' nature (pO_2, temperature, atmosphere). The concept may be extended to other perovskites since A-site vacancies can be accommodated in various concentrations and for a wide variety of B-site cations[34–43], and, potentially transferred to other oxide systems.

We have recently exemplified the use of the exsolution phenomenon to design high temperature steam electrolysis (HTSE) cathodes for H_2 production (e.g. $La_{0.4}Sr_{0.4}M_xTi_{1-x}O_{3-\gamma}$, M = Fe, Ni)[44]. The exsolution of metallic nanoparticles which occurred in situ during operation was found to coincide with a dramatic (absolute) drop in the steam electrolysis (i.e. water splitting) onset potential, from -1.21 V for the undoped perovskite to -0.98 V for the Fe-doped perovskite and further down to -0.63 V for the Ni-doped perovskite [44]. Similarly doped A-site stoichiometric analogues only showed modest decrease in HTSE potential. Thus, this provides proof of concept that remarkable increase in electrocatalytic activity may be achieved through this phenomenon.

Finally, the results presented here on cleaved samples vividly illustrate that native perovskite surfaces are preferentially A-site (rich) terminated to the detriment of the B-sites which are the sites generally occupied by catalytically active cations. As such, any assessment of perovskite surface properties based on an ideal bulk-like terminated surface can be

anticipated to be fundamentally flawed and thus the true catalytic properties of many perovskites might have been underestimated.

Methods

All the materials discussed have been prepared by a modified solid state synthesis described in detail previously[12,45]. In order to prepare the porous samples (typically 40% porosity), the powders of the as-prepared materials were mixed with glassy carbon (~10-15% weight) and fired at 1380 ˚C for 6 h (slowly, ~2 deg/min, until 1000 ˚C, in order to burn the carbon). Reduction was carried out at various temperatures in a controlled atmosphere furnace supplied with dry or slightly humidified (~3%H_2O) 5% H_2/Ar, while oxidations were done in static air. Powder X-ray diffraction (XRD) was performed at room temperature on representative samples on a PANalytical Empyrean Diffractometer operated in reflection mode. Selected data were analyzed and refined using FullProf software. Scanning electron microscopy (SEM) images were collected by using a FEG-SEM. The extent of the reduction of the samples was evaluated by performing a redox cycle and weighing them before and after each step, as described previously[45]. The XPS experiments were carried out using a Kratos Axis Ultra-DLD photoelectron spectrometer. The data were analysed using CasaXPS software.

Acknowledgments

The authors thank the EPSRC, Supergen XIV Project Delivery of Sustainable Hydrogen (*EP/G01244X/1*) and the European Project METSAPP (FCH JU-GA 278257) for funding.

References

1. Yates, J. T. & Campbell, C. T. Surface chemistry: Key to control and advance myriad technologies. *Proc. Natl Acad. Sci. USA* **108,** 911–916 (2011).

2. Farmer, J. A. & Campbell, C. T. Ceria Maintains Smaller Metal Catalyst Particles by Strong Metal-Support Bonding. *Science* **329,** 933–936 (2010).
3. Gorte, R. J. & Vohs, J. M. Nanostructured anodes for solid oxide fuel cells. *Curr. Opin. Colloid. In.* **14,** 236–244 (2009).
4. Kim, J.-S. *et al.* Highly Active and Thermally Stable Core-Shell Catalysts for Solid Oxide Fuel Cells. *J. Electrochem. Soc.* **158,** B596 (2011).
5. Nishihata, Y. *et al.* Self-regeneration of a Pd-perovskite catalyst for automotive emissions control. *Nature* **418,** 164–167 (2002).
6. Tanaka, H. *et al.* The intelligent catalyst having the self-regenerative function of Pd, Rh and Pt for automotive emissions control. *Catal. Today* **117,** 321–328 (2006).
7. Madsen, B. D., Kobsiriphat, W., Wang, Y., Marks, L. D. & Barnett, S. A. Nucleation of nanometer-scale electrocatalyst particles in solid oxide fuel cell anodes. *J. Power Sources* **166,** 64–67 (2007).
8. Madsen, B. D., Kobsiriphat, W., Wang, Y., Marks, L. D. & Barnett, S. SOFC Anode Performance Enhancement through Precipitation of Nanoscale Catalysts. *ECS Trans.* **7,** 1339–1348 (2007).
9. Kobsiriphat, W., Madsen, B. D., Wang, Y., Marks, L. D. & Barnett, S. A. $La_{0.8}Sr_{0.2}Cr_{1-x}Ru_xO_{3-\delta}$–$Gd_{0.1}Ce_{0.9}O_{1.95}$ solid oxide fuel cell anodes: Ru precipitation and electrochemical performance. *Solid State Ionics* **180,** 257–264 (2009).
10. Bierschenk, D. M. *et al.* Pd-substituted (La,Sr)$CrO_{3-\delta}$–$Ce_{0.9}Gd_{0.1}O_{2-\delta}$ solid oxide fuel cell anodes exhibiting regenerative behavior. *J. Power Sources* **196,** 3089–3094 (2011).
11. Katz, M. B. *et al.* Reversible precipitation/dissolution of precious-metal clusters in perovskite-based catalyst materials: Bulk versus surface re-dispersion. *J. Catal.* **293,** 145–148 (2012).
12. Neagu, D. & Irvine, J. T. S. Structure and Properties of $La_{0.4}Sr_{0.4}TiO_3$ Ceramics for Use as Anode Materials in Solid Oxide Fuel Cells. *Chem. Mater.* **22,** 5042–5053 (2010).
13. Howard, C., Lumpkin, G., Smith, R. & Zhang, Z. Crystal structures and phase transition in the system $SrTiO_3$–$La_{2/3}TiO_3$. *J. Solid State Chem.* **177,** 2726–2732 (2004).
14. Battle, P., Bennett, J. E., Sloan, J., Tilley, R. J. D. & Vente, J. F. A-Site Cation-Vacancy Ordering in $Sr_{1-3x/2}La_xTiO_3$: A Study by HRTEM. *J. Solid State Chem.* **149,** 360–369 (2000).
15. Anderson, M. T., Vaughey, J. T. & Poeppelmeier, K. R. Structural similarities among oxygen-deficient perovskites. *Chem. Mater.* **5,** 151–165 (1993).
16. Wang, Z. L. & Kang, Z. C. *Functional and smart materials: structural evolution and structure analysis*. (Springer, 1998).
17. Bowden, M. E., Jefferson, D. A. & Brown, I. W. M. Determination of Layer Structure in $Sr_{1-x}La_xTiO_{3+0.5x}$ ($0 < x < 1$) Compounds by High-Resolution Electron Microscopy. *J. Solid State Chem.* **117,** 88–96 (1995).
18. Canales-Vázquez, J., Smith, M. J., Irvine, J. T. S. & Zhou, W. Studies on the Reorganization of Extended Defects with Increasing n in the Perovskite-Based $La_4Sr_{n-4}Ti_nO_{3n+2}$ Series. *Adv. Funct. Mater.* **15,** 1000–1008 (2005).
19. Ruddlesden, S. N. & Popper, P. New compounds of the K_2NiF_4 type. *Acta Crystallogr.* **10,** 538–539 (1957).
20. Ruiz-Morales, J. C. *et al.* Disruption of extended defects in solid oxide fuel cell anodes for methane oxidation. *Nature* **439,** 568–571 (2006).
21. Shannon, R. D. Revised effective ionic radii and systematic studies of interatomic distances in halides and chalcogenides. *Acta Crystall. A-Crys.* **32,** 751–767 (1976).
22. Horvath, G., Gerblinger, J., Meixner, H. & Giber, J. Segregation driving forces in perovskite titanates. *Sensor Actuat. B-Chem.* **32,** 93–99 (1996).
23. Noguera, C. Polar oxide surfaces. *J. Phys.: Condens. Mat.* **12,** R367–R410 (2000).
24. Deak, D. S. Strontium titanate surfaces. *Mater. Sci. Tech. Ser.* **23,** 127–136 (2007).

25. Bonnell, D. A. & Garra, J. Scanning probe microscopy of oxide surfaces: atomic structure and properties. *Rep. Prog. Phys.* **71,** 044501 (2008).
26. Szot, K. & Speier, W. Surfaces of reduced and oxidized $SrTiO_3$ from atomic force microscopy. *Phys. Rev. B* **60,** 5909–5926 (1999).
27. Szot, K., Speier, W., Carius, R., Zastrow, U. & Beyer, W. Localized Metallic Conductivity and Self-Healing during Thermal Reduction of $SrTiO_3$. *Phys. Rev. Lett.* **88,** 075508 (2002).
28. Islam, M. S. Computer modelling of defects and transport in perovskite oxides. *Solid State Ionics* **154-155,** 75–85 (2002).
29. Jalili, H., Han, J. W., Kuru, Y., Cai, Z. & Yildiz, B. New Insights into the Strain Coupling to Surface Chemistry, Electronic Structure, and Reactivity of $La_{0.7}Sr_{0.3}MnO_3$. *J. Phys. Chem. Lett.* **2,** 801–807 (2011).
30. Szot, K. *et al.* Nature of the surface layer in ABO_3-type perovskites at elevated temperatures. *Appl. Phys. A-Mater.* **62,** 335–343 (1996).
31. Konysheva, E., Blackley, R. & Irvine, J. T. S. Conductivity Behavior of Composites in the $La_{0.6}Sr_{0.4}CoO_{3\pm\delta}$ - CeO_2 System: Function of Connectivity and Interfacial Interactions. *Chem. Mater.* **22,** 4700–4711 (2010).
32. Miller, D. N. & Irvine, J. T. S. B-site doping of lanthanum strontium titanate for solid oxide fuel cell anodes. *J. Power Sources* **196,** 7323–7327 (2011).
33. Kröger, F. A. & Vink, H. J. in *Solid State Physics* (Frederick Seitz and David Turnbull) **3,** 307–435 (Academic Press, 1956).
34. Stevenson, J. W., Hallman, P. F., Armstrong, T. R. & Chick, L. A. Sintering Behavior of Doped Lanthanum and Yttrium Manganite. *J. Am. Cer. Soc.* **78,** 507–512 (1995).
35. Tao, S. & Irvine, J. T. S. A redox-stable efficient anode for solid-oxide fuel cells. *Nature Mater.* **2,** 320–323 (2003).
36. Boulfrad, S., Cassidy, M., Djurado, E., Irvine, J. T. S. & Jabbour, G. Pre-coating of LSCM perovskite with metal catalyst for scalable high performance anodes. *Int. J. Hydrogen Energ.* **38,** 9519–9524 (2013).
37. Chakhmouradian, A. R., Mitchell, R. H. & Burns, P. C. The A-site deficient ordered perovskite $Th_{0.25}[]_{0.75}NbO_3$: a re-investigation. *J. Alloy Compd.* **307,** 149–156 (2000).
38. Stevenson, J. W. *et al.* Effect of A-site cation nonstoichiometry on the properties of doped lanthanum gallate. *Solid State Ionics* **113-115,** 571–583 (1998).
39. Vashook, V., Zosel, J., Preis, W., Sitte, W. & Guth, U. A-deficient chromites-titanates with the perovskite-type structure: synthesis and electrical conductivity. *Solid State Ionics* **175,** 441–444 (2004).
40. Slater, P. R., Fagg, D. P. & Irvine, J. T. S. Synthesis and electrical characterisation of doped perovskite titanates as potential anode materials for solid oxide fuel cells. *J. Mater. Chem.* **7,** 2495–2498 (1997).
41. Inaguma, Y., Seo, A. & Katsumata, T. Synthesis and lithium ion conductivity of cubic deficient perovskites $Sr_{0.5+x}Li_{0.5-2x}[]_xTi_{0.5}Ta_{0.5}O_3$ and the La-doped compounds. *Solid State Ionics* **174,** 19–26 (2004).
42. Konysheva, E. Y., Xu, X. & Irvine, J. T. S. On the Existence of A-Site Deficiency in Perovskites and Its Relation to the Electrochemical Performance. *Adv. Mater.* **24,** 528–532 (2012).
43. Hansen, K. K. & Hansen, K. V. A-site deficient $(La_{0.6}Sr_{0.4})_{1-s}Fe_{0.8}Co_{0.2}O_{3-\delta}$ perovskites as SOFC cathodes. *Solid State Ionics* **178,** 1379–1384 (2007).
44. Tsekouras, G., Neagu, D. & Irvine, J. T. S. Step-change in high temperature steam electrolysis performance of perovskite oxide cathodes with exsolution of B-site dopants. *Energy Environ. Sci.* **6,** 256–266 (2012).
45. Neagu, D. & Irvine, J. T. S. Enhancing Electronic Conductivity in Strontium Titanates through Correlated A and B-Site Doping. *Chem. Mater.* **23,** 1607–1617 (2011).